

Effects of Herzberg–Teller vibronic coupling on coherent excitation energy transfer

Hou-Dao Zhang, Qin Qiao, Rui-Xue Xu, and YiJing Yan

Citation: *J. Chem. Phys.* **145**, 204109 (2016); doi: 10.1063/1.4968031

View online: <http://dx.doi.org/10.1063/1.4968031>

View Table of Contents: <http://aip.scitation.org/toc/jcp/145/20>

Published by the [American Institute of Physics](#)

Effects of Herzberg–Teller vibronic coupling on coherent excitation energy transfer

Hou-Dao Zhang,^{1,a)} Qin Qiao,² Rui-Xue Xu,¹ and YiJing Yan^{1,b)}

¹*Hefei National Laboratory for Physical Sciences at the Microscale and Department of Chemical Physics and Synergetic Innovation Center of Quantum Information and Quantum Physics and iChEM, University of Science and Technology of China, Hefei, Anhui 230026, China*

²*Discipline of Neuroscience and Department of Anatomy, Histology and Embryology, Shanghai Jiao Tong University School of Medicine, Shanghai 200025, China*

(Received 28 August 2016; accepted 7 November 2016; published online 28 November 2016)

In this work, we study the effects of **non-Condon vibronic coupling** on the quantum coherence of excitation energy transfer, via the exact dissipaton-equation-of-motion evaluations on excitonic model systems. Field-triggered excitation energy transfer dynamics and two dimensional coherent spectroscopy are simulated for both Condon and non-Condon vibronic couplings. Our results clearly demonstrate that the non-Condon vibronic coupling intensifies the dynamical electronic-vibrational energy transfer and enhances the total system-and-bath quantum coherence. Moreover, the hybrid bath dynamics for non-Condon effects enriches the theoretical calculation, and further sheds light on the interpretation of the experimental nonlinear spectroscopy. *Published by AIP Publishing.* [<http://dx.doi.org/10.1063/1.4968031>]

I. INTRODUCTION

The long-lived quantum beats in the coherent excitation energy transfer (EET) in biological light-harvesting systems have drawn plentiful attention in the past decade.^{1–4} Two dimensional (2D) spectroscopy studies indicate that both electronic and vibrational coherences and their entanglement are responsible for this phenomenon.^{5–10} This interpretation is confirmed by many theoretical works in the framework of the Franck–Condon approximation.^{11–17} In this approximation, many studies show that strong vibronic coupling even increases the quantum yield of the EET process.^{18–20} In the meanwhile, however, the non-Condon vibronic coupling is also proposed to enhance the quantum coherence in many organic and biological molecular systems.^{21–23} To obtain a better understanding of the origin of quantum coherence in EET dynamics, the interplay of the Condon and non-Condon vibronic coupling effects deserves more theoretical investigations.

In studying the vibronic coupling effects, we need an integrated theory to handle both the excitonic system and the vibrational environment. On the other hand, the nonlinear nature of 2D spectroscopy calls for non-perturbative and non-Markovian treatments, based on such as the hierarchical equations of motion (HEOMs) approach.^{24–34} However, HEOM focuses primarily on the reduced system only, despite it involves a vast number of auxiliary density operators, which are purely mathematical quantities. As an alternative exact approach for open systems, the recently developed dissipaton equation of motion (DEOM) theory^{35–37} provides a quasi-particle dissipaton picture for the hybrid bath, and identifies its dynamical quantities as multi-body dissipaton density

operators. In this manner, the DEOM is capable of treating both the system and hybrid bath dynamics non-perturbatively. On describing reduced system dynamics, the DEOM recovers the HEOM method.^{24–34} The optimized DEOM formalism with damped Brownian oscillators can be constructed for studying the system dynamics under the influence of solvent fluctuations and intramolecular vibrations.^{38–41} The DEOM further enables us to directly investigate the solvation bath dynamics. In fact, it has been successfully applied in studying a variety of Fano-type interferences,^{36,42,43} quantum transport current shot noise spectrum,³⁷ and solvent-induced non-Condon polarization effects.⁴⁴

In this work, we study the influence of non-Condon vibronic coupling on the coherent EET dynamics in excitonic model systems and compare it with the Condon counterpart, via the DEOM approach. In simulating the electronic excitation of the system, the vibrational coordinates are explicitly involved in the transition dipole moments. This accounts for the non-Condon vibronic coupling under the Herzberg–Teller approximation.^{21,45–48} We model these vibrational modes in terms of underdamped Brownian oscillators (BOs).^{39,41,49} The underlying non-Condon effects are therefore studied via the hybrid bath dynamics in the DEOM framework.⁴⁴ In the Franck–Condon approximation, however, the transition dipole moments are independent of nuclear coordinates and the underdamped BOs merely serve as the vibrational environment. Based on our simulations on field-triggered EET dynamics and coherent 2D spectroscopy, we conclude that the non-Condon vibronic coupling facilitates the dynamical electronic-vibrational energy transfer and enhances the total system-and-bath quantum coherence, at both cryogenic and room temperatures. While both the Condon and non-Condon vibronic coupling elongate the quantum beats, the non-Condon polarization improves the quantum yield of the excitonic system.

^{a)}hdz@ustc.edu.cn

^{b)}yanyj@ustc.edu.cn

This paper is organized as follows. In Sec. II, we first set up an excitonic multi-chromophore system and model its surrounding environment with multiple Brownian oscillators, then briefly review the DEOM method and exemplify its application on the hybrid bath dynamics for non-Condon polarization effects. In Sec. III, we present the simulation results of field-triggered EET dynamics and coherent 2D spectroscopy for excitonic dimer systems, and compare the non-Condon and Condon vibronic coupling effects. The temperature dependence of these two effects is also discussed. Finally, we conclude this work in Sec. IV.

Throughout this paper, we set $\hbar = 1$ and $\beta = 1/(k_B T)$, with k_B and T being the Boltzmann constant and temperature, respectively.

II. METHODOLOGY

A. Model setup

Consider an excitonic multi-chromophore system embedded in an equilibrated thermal bath. The total composite system-and-bath Hamiltonian is summarized as $H_T = H_S + H_{SB} + h_B$. The excitonic system Hamiltonian reads

$$H_S = \epsilon_g |g\rangle\langle g| + \sum_a (\epsilon_a + \lambda_a) |a\rangle\langle a| + \sum_{a \neq b} V_{ab} |a\rangle\langle b|. \quad (1)$$

Here, the ground state energy ϵ_g is often set to be zero, whereas the diagonal onsite energies, reorganization energies, and inter-site couplings denote $\{\epsilon_a\}$, $\{\lambda_a\}$, and $\{V_{ab}\}$. The electronic dipole moment of each chromophore is $\hat{\mu}_a = \mu_a(\mathbf{X}_a)(|g\rangle\langle a| + |a\rangle\langle g|)$, where the transition matrix element $\mu_a(\mathbf{X}_a)$ depends on the nuclear coordinates \mathbf{X}_a . This form in fact accounts for the non-Condon coupling under the Herzberg–Teller approximation.⁴⁶ In the Franck–Condon limit, $\mu_a(\mathbf{X}_a)$ becomes a constant without the dependence on \mathbf{X}_a .

The thermal bath is modeled as numerous harmonic oscillators, $h_B = \sum_j \omega_j (p_j^2 + x_j^2)/2$, and the system-bath coupling takes the factorization form, i.e.,

$$H_{SB} = \sum_a \hat{Q}_a \hat{F}_a, \quad (2)$$

where $\hat{Q}_a = |a\rangle\langle a|$ is a system operator and $\hat{F}_a = \sum_j c_{aj} x_j$ is a linear collective bath operator. The bath influence on the reduced system can be entirely characterized by the hybrid bath spectral density $J_{ab}(\omega) = \frac{\pi}{2} \sum_j c_{aj}^2 \delta(\omega - \omega_j)$ or the macroscopic bare-bath correlation function (setting $t > 0$ hereafter),

$$\langle \hat{F}_a(t) \hat{F}_b(0) \rangle_B = \frac{1}{\pi} \int_{-\infty}^{\infty} d\omega \frac{e^{-i\omega t} J_{ab}(\omega)}{1 - e^{-\beta\omega}} \approx \sum_k \eta_{abk} e^{-\gamma_k t}, \quad (3)$$

with $\hat{F}_a(t) = e^{ih_B t} \hat{F}_a e^{-ih_B t}$ being a Gaussian stochastic variable in the h_B -interaction picture. The first identity is the fluctuation–dissipation theorem,^{50,51} while the second involves the parameterization of $J_{ab}(\omega)$ and certain sum-over-pole expansion of Bose function, $f^{\text{Bose}}(\omega) = (1 - e^{-\beta\omega})^{-1}$, followed by the Cauchy contour integral. The time-reversal correspondence to Eq. (3) reads

$$\langle \hat{F}_b(0) \hat{F}_a(t) \rangle_B = \langle \hat{F}_a(t) \hat{F}_b(0) \rangle_B^* = \sum_k \eta_{ab\bar{k}}^* e^{-\gamma_k t}. \quad (4)$$

The second expression, where the associate index \bar{k} goes with $\gamma_{\bar{k}} = \gamma_k^*$, reflects the fact that γ_k and γ_k^* must both appear if they are complex. Apparently, $\bar{k} = k$ for a real γ_k .

For the bath spectral density, we adopt the multiple Brownian oscillators (BOs) model. It can describe optically active vibronic coupling via the underdamped BO mode and also energy fluctuation via strongly overdamped Drude dissipation. For simplicity, we omit the subscript of different dissipative modes to the end of this subsection. An individual BO spectral density reads⁵²

$$J_{\text{BO}}(\omega) = \frac{2\lambda_{\text{BO}}\zeta_{\text{BO}}\omega_{\text{BO}}^2\omega}{(\omega^2 - \omega_{\text{BO}}^2)^2 + \zeta_{\text{BO}}^2\omega^2}, \quad (5)$$

with λ_{BO} , ω_{BO} , and ζ_{BO} being the reorganization energy, vibrational frequency, and the phonon linewidth, respectively. The Huang–Rhys factor that reflects the exciton-phonon coupling strength is defined as $S = \lambda_{\text{BO}}/\omega_{\text{BO}}$ in the free-oscillator limit. The underdamped BO is characterized by $\zeta_{\text{BO}}/2 < \omega_{\text{BO}}$, and is often adopted to describe intramolecular vibrations. In the strongly overdamped region ($\zeta_{\text{BO}}/2 \gg \omega_{\text{BO}}$), Eq. (5) recovers the Drude form,^{41,49}

$$J_{\text{D}}(\omega) = \frac{2\lambda_{\text{D}}\gamma_{\text{D}}\omega}{\omega^2 + \gamma_{\text{D}}^2}, \quad (6)$$

with $\lambda_{\text{D}} = \lambda_{\text{BO}}$ and $\gamma_{\text{D}} = \omega_{\text{BO}}^2/\zeta_{\text{BO}}$. This spectral density is often used to model diffusive solvent fluctuations.^{39,40} In more realistic cases, the bath spectral densities might be characterized by Ohmic and/or super-Ohmic models.^{16,53} Numerical bath decompositions, such as the Meier–Tannor scheme,⁵⁴ can be adopted, which fit the original spectral density with a set of Lorentzians and facilitate the construction of DEOM/HEOM formalism.⁵⁵

B. The DEOM theory

In DEOM, the dissipaton decomposition of the hybridization bath operator \hat{F}_a follows

$$\hat{F}_a = \sum_k \hat{f}_{ak}. \quad (7)$$

Each dissipaton \hat{f}_{ak} corresponds to an individual exponential term in Eq. (3) or Eq. (4), described by

$$\begin{aligned} \langle \hat{f}_{ak}(t) \hat{f}_{bj}(0) \rangle_B^> &= \delta_{kj} \eta_{abk} e^{-\gamma_k t}, \\ \langle \hat{f}_{bj}(0) \hat{f}_{ak}(t) \rangle_B^< &= \delta_{kj} \eta_{ab\bar{k}}^* e^{-\gamma_k t}. \end{aligned} \quad (8)$$

The same damping exponent along the time forward (>) and backward (<) pathways highlights the diffusive nature of dissipatons.^{35,36} The above dissipaton description of bath correlation is mathematically valid, and can be further simplified with $\bar{k} = k$ for individual real-colored dissipaton in the Smoluchowski diffusive limit. For an underdamped BO, there exists a pair of dissipatons with complex conjugate damping exponents, $\gamma_{\bar{k}} = \gamma_k^*$. In this case, a more physically comprehensive interpretation that involves second quantization treatment can be put forward, which neatly reflects the quasi-particle nature of dissipatons. Detailed derivation and interpretation on this issue will be published elsewhere.

Dynamical variables of DEOM are the so-called *dissipaton density operators* (DDOs), defined as^{35,36}

$$\rho_{\mathbf{n}}^{(n)}(t) \equiv \text{tr}_B \left[\left(\prod_{ak} \hat{f}_{ak}^{n_{ak}} \right)^{\circ} \rho_T(t) \right]. \quad (9)$$

Here, $\rho_T(t)$ is the total system-and-bath composite density operator, and tr_B denotes the trace over bath degrees of freedom. The dissipaton operators' product inside the circled parentheses is *irreducible*. The notation here follows (c-number) $^{\circ} = 0$, and bosonic dissipatons are permutable, $(\hat{f}_{ak}\hat{f}_{bj})^{\circ} = (\hat{f}_{bj}\hat{f}_{ak})^{\circ}$. In Eq. (9), $\mathbf{n} \equiv \{n_{ak}\}$ and $n \equiv \sum_{ak} n_{ak}$, with n_{ak} being the participation number of individual dissipaton. Apparently, $\rho^{(0)} = \text{tr}_B \rho_T = \rho_S$ is the reduced system density operator. Those $\{\rho_{\mathbf{n}}^{(n>0)}\}$ specify n -body dissipaton configurations, which account for the hybrid bath dynamics. For later use, we denote also the adjacent ($n \pm 1$)-body quantities, $\rho_{\mathbf{n}_{ak}^{\pm}}^{(n+1)}$ and $\rho_{\mathbf{n}_{ak}^{\pm}}^{(n-1)}$, with the index \mathbf{n}_{ak}^{\pm} differing from \mathbf{n} by $n_{ak} \pm 1$, at the specified dissipaton. The multi-body DDOs form the hierarchy structure and they are dynamically linked together via the irreducible notation in Eq. (9) and the generalized Wick's theorem,^{35,36}

$$\begin{aligned} & \text{tr}_B \left[\left(\prod_{ak} \hat{f}_{ak}^{n_{ak}} \right)^{\circ} \hat{f}_{bj} \rho_T \right] \\ &= \rho_{\mathbf{n}_{bj}^{+}}^{(n+1)} + \sum_{ak} n_{ak} \langle \hat{f}_{ak} \hat{f}_{bj} \rangle_B^{\circ} \rho_{\mathbf{n}_{ak}^{-}}^{(n-1)} \\ &= \rho_{\mathbf{n}_{bj}^{+}}^{(n+1)} + \sum_a n_{aj} \eta_{abj} \rho_{\mathbf{n}_{aj}^{-}}^{(n-1)} \end{aligned} \quad (10)$$

and

$$\begin{aligned} & \text{tr}_B \left[\left(\prod_{ak} \hat{f}_{ak}^{n_{ak}} \right)^{\circ} \rho_T \hat{f}_{bj} \right] \\ &= \rho_{\mathbf{n}_{bj}^{+}}^{(n+1)} + \sum_{ak} n_{ak} \langle \hat{f}_{bj} \hat{f}_{ak} \rangle_B^{\circ} \rho_{\mathbf{n}_{ak}^{-}}^{(n-1)} \\ &= \rho_{\mathbf{n}_{bj}^{+}}^{(n+1)} + \sum_a n_{aj} \eta_{abj}^{*} \rho_{\mathbf{n}_{aj}^{-}}^{(n-1)}, \end{aligned} \quad (11)$$

where we use the following relation [cf. Eq. (8)]:

$$\begin{aligned} \langle \hat{f}_{ak} \hat{f}_{bj} \rangle_B^{\circ} &\equiv \langle \hat{f}_{ak}(0+) \hat{f}_{bj} \rangle = \delta_{kj} \eta_{abk}, \\ \langle \hat{f}_{bj} \hat{f}_{ak} \rangle_B^{\circ} &\equiv \langle \hat{f}_{bj} \hat{f}_{ak}(0+) \rangle = \delta_{kj} \eta_{abk}^{*}. \end{aligned}$$

Equations (10) and (11) accomplish the most significant part of the DEOM theory. They are adopted not only in deriving the fundamental DEOM formalism below, but also for evaluating dynamics of hybrid bath quantities.^{35,36,44}

The DEOM formalism can be derived via the established dissipaton algebra.^{35,36} The final results read

$$\begin{aligned} \dot{\rho}_{\mathbf{n}}^{(n)} &= -[i\mathcal{L}_S + \sum_{ak} n_{ak} \gamma_k] \rho_{\mathbf{n}}^{(n)} \\ &\quad - i \sum_{ak} [\mathcal{A}_a \rho_{\mathbf{n}_{ak}^{+}}^{(n+1)} + n_{ak} \mathcal{C}_{ak} \rho_{\mathbf{n}_{ak}^{-}}^{(n-1)}], \end{aligned} \quad (12)$$

where $\mathcal{L}_S \hat{O} = [H_S, \hat{O}]$ defines the system Liouvillian and

$$\begin{aligned} \mathcal{A}_a \hat{O} &\equiv [\hat{Q}_a, \hat{O}], \\ \mathcal{C}_{ak} \hat{O} &\equiv \sum_b (\eta_{abk} \hat{Q}_b \hat{O} - \eta_{abk}^{*} \hat{O} \hat{Q}_b). \end{aligned} \quad (13)$$

Equation (12) recovers the HEOM formalism,^{24–32} constructed originally on the basis of Feynman-Vernon influence functional path integral expression.⁵⁶ Nevertheless, the DDOs are now responsible for hybrid bath dynamics instead of being pure mathematical tools in HEOM.^{24–32} This fact has been justified by many DEOM-based studies on Fano interference, current shot noise, and solvent-induced non-Condon polarization phenomena.^{36,37,42,44} In this work, we also illustrate the DEOM study of hybrid bath dynamics for non-Condon vibronic coupling effects.

Denote $\rho \equiv \{\rho^{(0)}, \rho_{\mathbf{n}}^{(n)}\}$ the DEOM-space state vector. Similarly, $\hat{A} \equiv \{\hat{A}^{(0)}, \hat{A}_{\mathbf{n}}^{(n)}\}$ is introduced as the DEOM-space extension of a dynamical variable, \hat{A} , in the system-and-hybrid-bath subspace. According to $\text{Tr}(\hat{A} \rho_T) = \text{Tr}(\hat{A} \rho_T)$, we immediately obtain the DEOM in the Heisenberg picture,^{39,57,58}

$$\begin{aligned} \dot{\hat{A}}_{\mathbf{n}}^{(n)} &= -\hat{A}_{\mathbf{n}}^{(n)} (i\mathcal{L}_S + \sum_{ak} n_{ak} \gamma_k) \\ &\quad - i \sum_{ak} [\hat{A}_{\mathbf{n}_{ak}^{+}}^{(n-1)} \mathcal{A}_a + (n_{ak} + 1) \hat{A}_{\mathbf{n}_{ak}^{+}}^{(n+1)} \mathcal{C}_{ak}]. \end{aligned} \quad (14)$$

The involving superoperators in Heisenberg picture read $\hat{\mathcal{O}} \mathcal{L}_S \equiv [\hat{\mathcal{O}}, H_S]$ and

$$\begin{aligned} \hat{\mathcal{O}} \mathcal{A}_a &\equiv [\hat{\mathcal{O}}, \hat{Q}_a], \\ \hat{\mathcal{O}} \mathcal{C}_{ak} &\equiv \sum_b (\eta_{abk} \hat{\mathcal{O}} \hat{Q}_b - \eta_{abk}^{*} \hat{Q}_b \hat{\mathcal{O}}). \end{aligned} \quad (15)$$

The Heisenberg picture dynamics is equivalent to the Schrödinger picture counterpart, since the expectation value of any physical observable is of prescription invariance. Furthermore, the mixed Heisenberg-Schrödinger picture dynamics has been implemented in the DEOM/HEOM method, for efficient evaluations of nonlinear correlation and response functions.^{44,57} In addition, an efficient and prescription invariance truncation scheme is also developed for the DEOM/HEOM evolution in both Schrödinger and Heisenberg pictures.^{42,44}

C. The non-Condon dynamics via DEOM approach

To exemplify the DEOM application in bath dynamics, we study the non-Condon vibronic coupling effects in the linear absorption spectroscopy, where the polarizable vibrational modes are treated in terms of underdamped BOs in the hybrid bath.

Under the dipole approximation, the matter-field interaction is given by $H_{\text{mat-fld}}(t) = -\hat{V} \varepsilon(t)$, with the external field being $\varepsilon(t)$, and the total dipole moment

$$\hat{V} = \sum_a \mu_a(\mathbf{X}_a) \hat{D}_a. \quad (16)$$

Here, $\mu_a(\mathbf{X}_a)$ and $\hat{D}_a = |g\rangle\langle a| + |a\rangle\langle g|$ are the transition matrix element and electronic operator, respectively. The non-Condon vibronic coupling under the Herzberg-Teller approximation involves the nuclear coordinate dependence in the dipole moment, for which we consider the simple form

$$\mu_a(\mathbf{X}_a) = \mu_a + \mu'_a \hat{F}_a^{\text{BO}} / \lambda_{\text{BO}}, \quad (17)$$

where the hybrid bath operator \hat{F}_a^{BO} is only associated with the underdamped BO. In Eq. (17), μ_a and μ'_a represent the strength of the Condon and non-Condon transition dipoles, whereas

the effective nuclear coordinate $\hat{F}_a^{\text{BO}}/\lambda_{\text{BO}}$ is dimensionless. In the Franck–Condon limit, the dipole moment element is a constant, with $\mu_a(\mathbf{X}_a) = \mu_a$.

The linear absorption lineshape is simulated via

$$I(\omega) = \text{Re} \int_0^\infty dt e^{i\omega t} \text{Tr}[\hat{V} e^{-i\mathcal{L}_T t} \hat{V} \rho_T^{\text{eq}}] \\ = \text{Re} \int_0^\infty dt e^{i\omega t} \langle \langle \hat{V} | e^{-i\mathcal{L}_T t} \hat{V} | \rho^{\text{eq}} \rangle \rangle. \quad (18)$$

The Fourier integrand in the first line defines the dipole-dipole correlation in the total system-and-bath space, with ρ_T^{eq} being the equilibrated total density operator and \mathcal{L}_T the total Liouvillian, while the one in the second line is the DEOM-space equivalence. In numerical implementation, the DEOM-space evaluation is carried out following the established dissipaton algebra,^{35,36,44} including the dissipaton decomposition of bath operator in Eq. (7), the generalized Wick's theorem in Eqs. (10) and (11), and the ordinary DEOM evolution via Eq. (12).

Figure 1 depicts the linear absorption results for an excitonic monomer under the influence of a bare underdamped BO mode. In fact, for such two-level system, the linear absorption profile is analytically solvable, resulting in

$$I(\omega) = (\mu + \mu' \Delta\omega/\lambda_{\text{BO}})^2 I_0(\omega). \quad (19)$$

Here, $\Delta\omega = \omega - \epsilon$, where ϵ is the excitonic onsite energy, and $I_0(\omega) = \text{Re} \int_0^\infty dt e^{i\Delta\omega t - g(t)}$ denotes the result in the Franck–Condon limit, with $g(t)$ being the well-known lineshape function for the simple two-level system.⁵² We have verified that the analytical solutions are identical to the results in Fig. 1. In the Condon limit, which corresponds to $\mu' = 0$, we observe the sharp zero-phonon transition peak at $\Delta\omega = 0$, and small vibrational signals at $\Delta\omega = \pm\omega_{\text{B}}$. As μ' is tuned up, i.e., the non-Condon transition increases, the zero-phonon transition peak decreases and vibrational excitations become prominent. The absorption lineshape would develop into two continuum bands when BO goes to the super-overdamped region. This is equivalent to the solvent-induced non-Condon polarization effect, which has already been studied in our previous work.⁴⁴

Figure 2 presents the linear absorption results that additionally involve the solvent environment described by Drude dissipation, while all other parameters (except μ') remain the same as Fig. 1. Due to the solvent modulation, both electronic

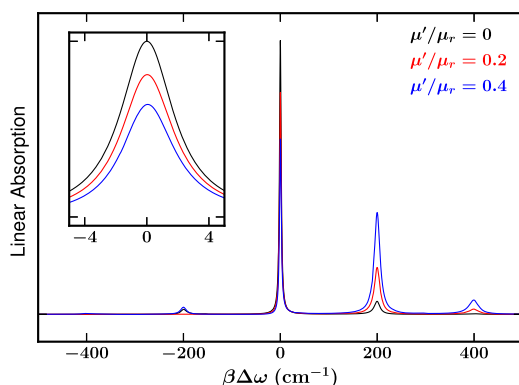


FIG. 1. Linear absorption lineshapes of an excitonic monomer under the influence of an underdamped BO at 298 K, with various μ' and fixed $\mu = \mu_r$, where μ_r is the reference dipole strength. The parameters of the underdamped BO are $S = 0.1$, $\omega_{\text{BO}} = 200 \text{ cm}^{-1}$, and $\zeta_{\text{BO}} = 10 \text{ cm}^{-1}$.

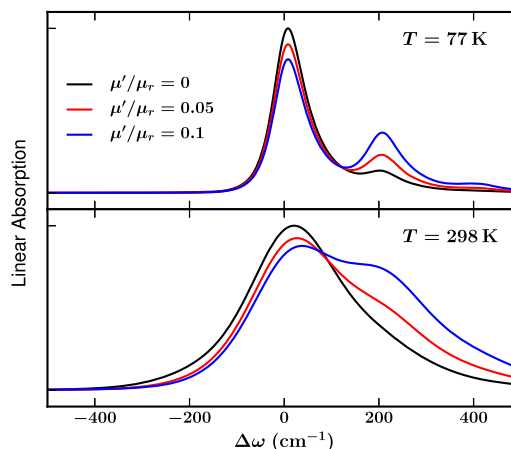


FIG. 2. Linear absorption lineshapes of the excitonic monomer in Fig. 1 with additional solvent environment at 77 and 298 K, for various non-Condon transition strengths. In addition to the underdamped BO, the solvent environment is modeled by a Drude spectral density, with the parameters $\lambda_{\text{D}} = 40 \text{ cm}^{-1}$ and $\gamma_{\text{D}} = 100 \text{ cm}^{-1}$. The overall reorganization energy is $\lambda = \lambda_{\text{BO}} + \lambda_{\text{D}} = 60 \text{ cm}^{-1}$.

and vibrational peaks are now much broader than the ones in Fig. 1, which only contains the vibronic coupling modeled by underdamped BO. Apparently, the non-Condon effects are more prominent at the room temperature (298 K). At 77 K, the increase of μ' diminishes the zero-phonon transition and strengthens the vibrational peaks on the blue side, but does not change the peak positions significantly. At 298 K, the excitonic peak becomes much broader and shifted to the blue side, while the vibrational one gradually appears, as the μ' increases.

Last but not least, we note that the appearance of the vibrational peaks may be caused by not only the non-Condon transition but also the strong Franck–Condon vibronic coupling, see the similarity between Figs. 2 and 3. To distinguish the above two causes experimentally, one can examine the mirror symmetry between the absorption and emission spectroscopies.⁴⁵ While the Franck–Condon approximation results in symmetric lineshapes, the non-Condon effects preferentially enhance the vibrational peaks on the blue side in both the absorption and emission spectroscopies.

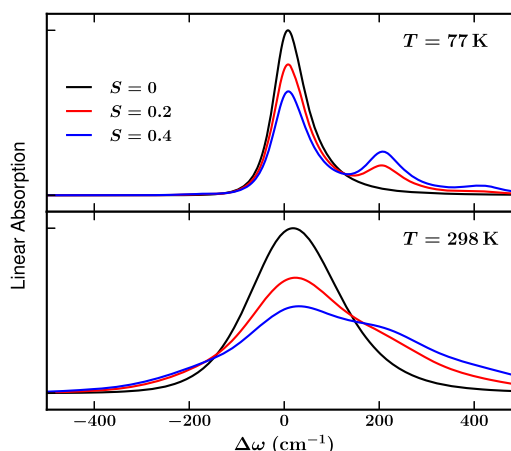


FIG. 3. Linear absorption lineshapes of the excitonic monomer in Fig. 2 in the Condon limit at 77 and 298 K, under various Huang-Rhys factors S .

III. RESULTS AND DISCUSSION

In this section, we discuss the simulation results of **field-triggered EET dynamics and 2D spectroscopy** for an excitonic dimer system. Each monomer is longitudinally subject to a diffusive solvent bath and a vibrational mode, which are characterized by a Drude model ($\lambda_D = 40 \text{ cm}^{-1}$ and $\gamma_D = 100 \text{ cm}^{-1}$), and an underdamped BO ($S = 0.1$, $\omega_{BO} = 200 \text{ cm}^{-1}$ and $\zeta_{BO} = 10 \text{ cm}^{-1}$), respectively. The reorganization energy of each monomer is $\lambda_1 = \lambda_2 = \lambda_{BO} + \lambda_D = 60 \text{ cm}^{-1}$. The site energies are given by $\epsilon_1 + \lambda_1 = 12500 \text{ cm}^{-1}$ and $\epsilon_2 + \lambda_2 = 12300 \text{ cm}^{-1}$, and the dipole-dipole coupling is $V_{12} = -100 \text{ cm}^{-1}$. Without loss of generality, we assume the two sites have the same dipole strength and set $\mu_1 = \mu_2 = \mu_r$ for the Condon part and $\mu'_1/\mu_r = \mu'_2/\mu_r = 0.1$ for the non-Condon part [cf. Eq. (17)], with μ_r being the reference dipole strength.

A. Field-triggered excitation energy transfer dynamics

In Fig. 4, we report the field-triggered population dynamics at three different conditions, including the pure Drude dissipation without vibronic coupling, the one with Franck-Condon coupling, and the one with Herzberg-Teller coupling. It is observed that the time duration of the population oscillation is largely elongated by both Condon and non-Condon vibronic couplings. While the electronic coherence with pure Drude dissipation disappears within 500 fs, the vibronic coherence reaches above 1 ps. The oscillation is weakened but still noticeable as the temperature increases.

We also find that the non-Condon vibronic coupling enhances the quantum yield of the excitonic system, especially at the high temperature. In comparison, the Condon vibronic coupling does not vary the final population significantly, at least in the weak coupling regime.^{13,14,18–20} This finding highlights the dynamical interplay between excitation of the system and non-Condon polarization of the vibrational environment.

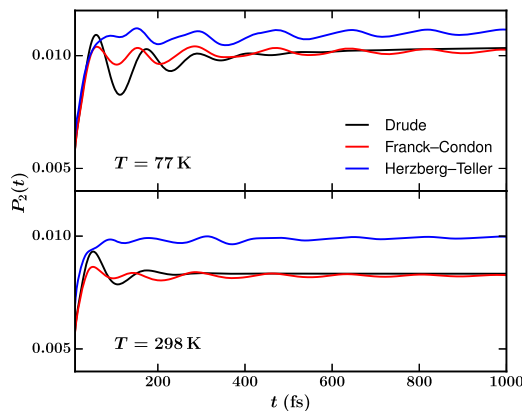


FIG. 4. **Field-triggered EET dynamics** for an excitonic dimer system at 77 and 298 K: the pure Drude dissipation without vibronic coupling (black), the one with Franck-Condon coupling (red), and the one with Herzberg-Teller coupling (blue). The pulse is characterized by a Gaussian envelope $\mu_r \varepsilon(t) = \frac{\theta}{\sqrt{2\pi}\sigma} \exp(-\frac{t^2}{2\sigma^2}) \cos(\omega_c t)$, where the reference dipole strength is μ_r , the flipping angle $\theta = 0.05\pi$, the temporal variance $\sigma = 6 \text{ fs}$, and the carrier frequency $\omega_c = 12400 \text{ cm}^{-1}$.

In the meanwhile, it is shown that these two kinds of vibronic couplings result in similar population oscillation, indicating that the non-Condon vibronic coupling retains the electronic coherence of the reduced system. On the other hand, the total quantum coherence, including contributions from both the reduced system and polarized vibrational environment, is enhanced, as discussed in Sec. III B of the 2D spectroscopy simulations.

B. Coherent two dimensional spectroscopy

To investigate the dynamical electronic-vibrational interaction and the involving Condon and non-Condon effects, we further simulate the 2D spectroscopy for the dimer system. 2D coherent spectroscopy is a four-wave-mixing technique.^{52,59,60} The multi-chromophore system is excited by three time-ordered laser pulses (with wavevectors \mathbf{k}_1 , \mathbf{k}_2 , and \mathbf{k}_3) separated by time interval t_1 and t_2 , and after a time-delay t_3 , the emitted signal is measured along the phase matching direction $\mathbf{k}_s = \pm \mathbf{k}_3 \pm \mathbf{k}_2 \pm \mathbf{k}_1$. In this work, we adopt the pump-probe configuration,^{52,59,60} and the simulated 2D spectrum is the direct summation of the rephasing $\mathbf{k}_I = \mathbf{k}_3 + \mathbf{k}_2 - \mathbf{k}_1$ and non-rephasing $\mathbf{k}_{II} = \mathbf{k}_3 - \mathbf{k}_2 + \mathbf{k}_1$ signals, $S_{\text{total}} = S_{\mathbf{k}_I} + S_{\mathbf{k}_{II}}$. For simplicity, we adopt the rotating wave approximation and the impulsive limit.^{52,59,60}

The rephasing $S_{\mathbf{k}_I}$ and non-rephasing $S_{\mathbf{k}_{II}}$ signals are given by^{52,57}

$$S_{\mathbf{k}_{I/II}}(\omega_3, t_2, \omega_1) = \text{Re} \int_0^\infty dt_3 \int_0^\infty dt_1 e^{i(\omega_3 t_3 \mp \omega_1 t_1)} \times R_{\mathbf{k}_{I/II}}(t_3, t_2, t_1) \quad (20)$$

and related, respectively, to the nonlinear optical correlation functions

$$\begin{aligned} R_{\mathbf{k}_I} &= R_2 + R_3 + R_5 & (\text{rephasing}), \\ R_{\mathbf{k}_{II}} &= R_1 + R_4 + R_6 & (\text{non-rephasing}). \end{aligned} \quad (21)$$

In Eq. (21), the six Liouville-space pathways are expressed as^{44,57}

$$\begin{aligned} R_1 &= \langle \langle \hat{V}_{ge}(t_3) | \bar{V}_{eg} \mathcal{G}_{ee}(t_2) \bar{V}_{ge} \mathcal{G}_{eg}(t_1) \bar{V}_{eg} | \rho_{T,gg}^{\text{eq}} \rangle \rangle, \\ R_2 &= \langle \langle \hat{V}_{ge}(t_3) | \bar{V}_{eg} \mathcal{G}_{ee}(t_2) \bar{V}_{eg} \mathcal{G}_{ge}(t_1) \bar{V}_{ge} | \rho_{T,gg}^{\text{eq}} \rangle \rangle, \\ R_3 &= \langle \langle \hat{V}_{ge}(t_3) | \bar{V}_{eg} \mathcal{G}_{gg}(t_2) \bar{V}_{eg} \mathcal{G}_{ge}(t_1) \bar{V}_{ge} | \rho_{T,gg}^{\text{eq}} \rangle \rangle, \\ R_4 &= \langle \langle \hat{V}_{ge}(t_3) | \bar{V}_{eg} \mathcal{G}_{gg}(t_2) \bar{V}_{ge} \mathcal{G}_{eg}(t_1) \bar{V}_{eg} | \rho_{T,gg}^{\text{eq}} \rangle \rangle, \\ R_5 &= -\langle \langle \hat{V}_{ef}(t_3) | \bar{V}_{fe} \mathcal{G}_{ee}(t_2) \bar{V}_{eg} \mathcal{G}_{ge}(t_1) \bar{V}_{ge} | \rho_{T,gg}^{\text{eq}} \rangle \rangle, \\ R_6 &= -\langle \langle \hat{V}_{ef}(t_3) | \bar{V}_{fe} \mathcal{G}_{ee}(t_2) \bar{V}_{ge} \mathcal{G}_{eg}(t_1) \bar{V}_{eg} | \rho_{T,gg}^{\text{eq}} \rangle \rangle. \end{aligned} \quad (22)$$

Here, all the involving operators and the propagator $\mathcal{G}(t) \equiv e^{-i\hat{\mathcal{L}}_T t}$ are in their block forms subscripted by “uv,” where $u, v \in \{g, e, f\}$, with $|g\rangle$, $|e\rangle$, and $|f\rangle$ specifying the ground, singly excited and, doubly excited electronic manifolds, respectively.⁵⁷ The efficient evaluation of the DEOM-space equivalence of Eq. (22) follows Refs. 44 and 57. In our simulations, all parameters remain the same as those in Fig. 4.

Figure 5 demonstrates the simulated 2D spectroscopy at 77 K under three circumstances, i.e., the pure Drude dissipation without vibronic coupling, the one with Franck–Condon coupling, and the one with Herzberg–Teller coupling. In the presence of the vibronic coupling, vibrational peaks on both the diagonal and off-diagonal are observed, while the exciton-exciton off-diagonal peak is concealed. In particular, an electronic-vibrational cross peak (CP) appears right to the excitonic diagonal peak (DP) with the frequency difference around ω_{BO} , as observed in the middle- and bottom-left panels of Fig. 5. It suggests that this CP measures the cross correlation between the first and the zeroth vibrational levels within the excited electronic state. With the non-Condon vibronic coupling, the above vibrational signals are more prominent. The right panels show the t_2 time-evolution of the signals along the dashed horizontal line, covering both the excitonic DP and the electronic-vibrational CP. With the vibronic coupling, the duration of the quantum beats is elongated obviously. As shown in the middle- and bottom-right panels, the vibronic CPs oscillate for at least 1 ps with both Condon and non-Condon vibronic couplings. For DPs, however, the oscillation with non-Condon coupling is more persistent than that with Condon coupling. Moreover, the non-Condon coupling results in a larger oscillation amplitude. Evidently, the vibronic coupling facilitates the quantum coherence in the EET dynamics. In particular, the non-Condon transition greatly enhances the excitation of higher vibrational levels in the excited state. The subsequent vibrational energy relaxation preserves the

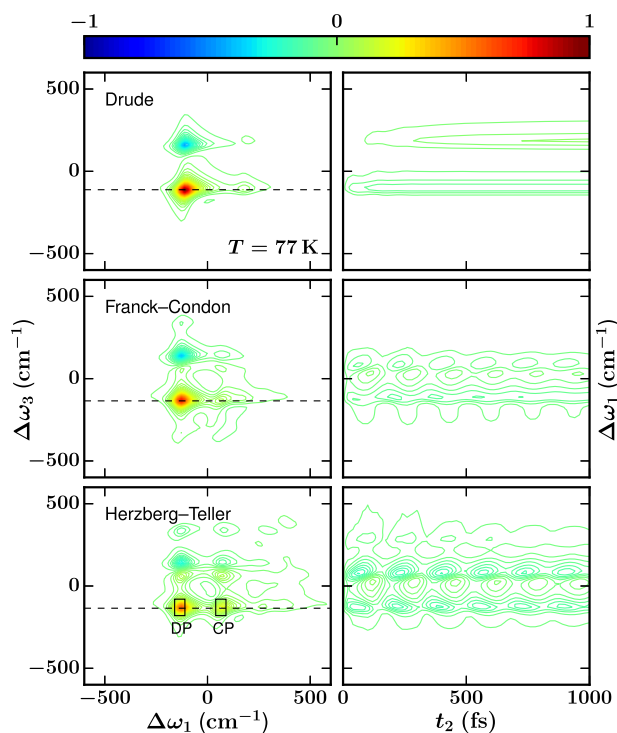


FIG. 5. Two dimensional spectroscopy of the dimer system at 77 K, for the pure Drude dissipation without vibronic coupling (top), the one with Franck–Condon coupling (middle), and the one with Herzberg–Teller coupling (bottom). The left panels show the 2D signals at $t_2 = 0$, while the right panels show the t_2 dynamics of the signals along the dashed horizontal line. We set $\Delta\omega_k = \omega_k - (\epsilon_1 + \epsilon_2)/2$ for $k = 1$ and 3. All the results are scaled by the maximum of the pure Drude results. In the right panels, the initial values at $t_2 = 0$ have been subtracted.

long-lived coherence and amplifies the oscillation amplitudes in 2D spectroscopy.

In comparison with the results at 77 K, the 2D signals at 298 K are much broader, and the electronic and vibrational excitation peaks are not well separated, see Fig. 6. However, in the right panels, we observe similar dynamics of the excitonic DPs and electronic-vibrational CPs as those at 77 K. Apparently, the vibrational energy relaxation at 298 K is more prominent than that at 77 K, see the middle-right and bottom-right panels in Figs. 5 and 6 for comparison.

In Fig. 7, we further compare the oscillation amplitudes at the cryogenic and room temperatures of the excitonic DPs and vibronic CPs along t_2 , with all curves being scaled by the maximum of the 2D spectroscopy with pure Drude dissipation at the cryogenic temperature (77 K). In both the Condon and non-Condon couplings, the quantum beats of the DPs and CPs last for more than 2 ps, and their amplitudes are still noticeable at room temperature (298 K), about one-third of those at 77 K. In contrast, the quantum beats from purely electronic transitions are very short-lived, i.e., its coherence only lasts for 300 fs at 77 K and becomes even more transient at 298 K. Moreover, the non-Condon vibronic coupling further intensifies the vibrational oscillation amplitudes dramatically at both temperatures, in comparison with the Condon results.

Clearly, 2D spectroscopy detects both the excitonic system and the polarized vibrational environment. Our simulation results indicate that the vibronic coupling plays a dominant role in preserving the long-lived quantum beats, whereas the purely electronic coherence has a minor contribution. This persistent quantum coherence is present at both cryogenic and room temperatures. Moreover, in comparison with the Condon counterpart, the non-Condon vibronic coupling

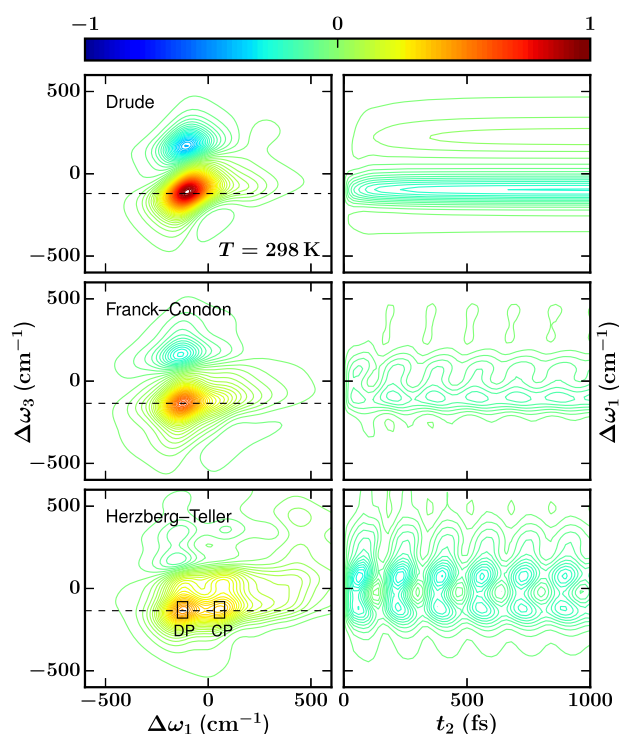


FIG. 6. Two dimensional spectroscopy of the dimer system at 298 K. All the rest parameters are the same as those in Fig. 5.

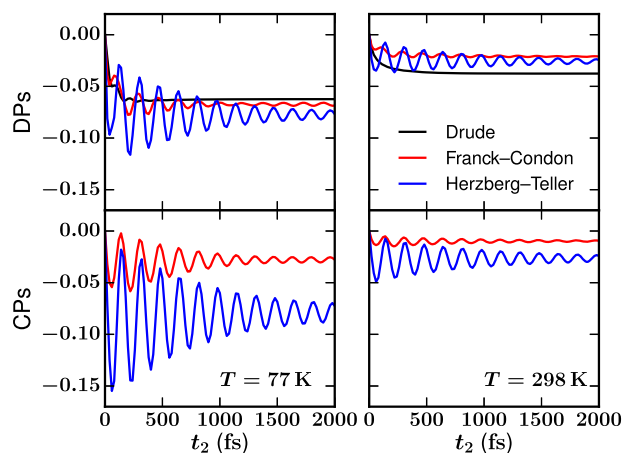


FIG. 7. Amplitudes of the DPs and CPs along time interval t_2 in the previous 2D spectroscopy at both 77 and 298 K: the pure Drude dissipation (black, for DPs only), the one with Franck-Condon coupling (red), and the one with Herzberg-Teller coupling (blue). All the curves are scaled by the maximum of pure Drude results at 77 K and then shifted vertically to make the initial values 0.

greatly enhances the excitation of the higher vibrational levels in the excited electronic state, and the subsequent vibrational relaxation leads to the stronger quantum beats, in the coherent 2D spectroscopy.

IV. CONCLUSION

In this work, we investigate the non-Condon vibronic coupling effects on the quantum coherence of the EET dynamics, via the non-perturbative DEOM simulations on excitonic model systems. Evidently, the DEOM is a unique theory in studying both the reduced system and the hybrid bath dynamics as well as their correlated quantum entanglement. Our simulations on field-triggered EET dynamics and coherent 2D spectroscopy show that the vibronic coupling elongates the quantum beats at both cryogenic and room temperatures. In particular, the non-Condon vibronic coupling facilitates the electronic-vibrational energy transfer and dramatically enhances the total system-and-bath quantum coherence. This work provides an insightful investigation on the origin of the quantum coherence, and may enrich the interpretation of the experimental nonlinear spectroscopy.

ACKNOWLEDGMENTS

The support from the Natural Science Foundation of China (Grant Nos. 21373191 and 21633006), the Fundamental Research Funds for the Central Universities (Grant No. 2030020028), and the Ministry of Science and Technology (Grant No. 2016YFA0400900) is gratefully acknowledged. In our numerical implementation, the Armadillo library⁶¹ was used.

¹G. S. Engel *et al.*, *Nature* **446**, 782 (2007).

²Y.-C. Cheng and G. R. Fleming, *J. Phys. Chem. A* **112**, 4254 (2008).

³G. Panitchayangkoon *et al.*, *Proc. Natl. Acad. Sci. U. S. A.* **107**, 12766 (2010).

⁴M. B. Plenio, J. Almeida, and S. F. Huelga, *J. Chem. Phys.* **139**, 235102 (2013).

- ⁵D. B. Turner, K. E. Wilk, P. M. G. Curmi, and G. D. Scholes, *J. Phys. Chem. Lett.* **2**, 1904 (2011).
- ⁶R. Tempelaar, T. L. C. Jansen, and J. Knoester, *J. Phys. Chem. B* **118**, 12865 (2014).
- ⁷V. Butkus, L. Valkunas, and D. Abramavicius, *J. Chem. Phys.* **140**, 034306 (2014).
- ⁸F. V. A. Camargo, H. L. Anderson, S. R. Meech, and I. A. Heisler, *J. Phys. Chem. A* **119**, 95 (2015).
- ⁹V. Balevičius *et al.*, *Phys. Chem. Chem. Phys.* **17**, 19491 (2015).
- ¹⁰H. G. Duan, A. G. Dijkstra, P. Nalbach, and M. Thorwart, *Phys. Rev. E* **92**, 042708 (2015).
- ¹¹T. Mančal *et al.*, *J. Phys. Chem. Lett.* **3**, 1497 (2012).
- ¹²V. Perlík, C. Lincoln, F. Šanda, and J. Hauer, *J. Phys. Chem. Lett.* **5**, 404 (2014).
- ¹³Y. Fujihashi, G. R. Fleming, and A. Ishizaki, *J. Chem. Phys.* **142**, 212403 (2015).
- ¹⁴D. M. Monahan, L. Whaley-Mayda, A. Ishizaki, and G. R. Fleming, *J. Chem. Phys.* **143**, 065101 (2015).
- ¹⁵H. G. Duan, P. Nalbach, V. I. Prokhorov, S. Mukamel, and M. Thorwart, *New J. Phys.* **17**, 072002 (2015).
- ¹⁶P. Nalbach, D. Braun, and M. Thorwart, *Phys. Rev. E* **84**, 041926 (2011).
- ¹⁷P. Nalbach and M. Thorwart, *J. Phys. B: At., Mol. Opt. Phys.* **45**, 154009 (2012).
- ¹⁸P. Nalbach, C. A. Mujica-Martinez, and M. Thorwart, *Phys. Rev. E* **91**, 022706 (2015).
- ¹⁹H. G. Duan *et al.*, *J. Phys. Chem. B* **119**, 12017 (2015).
- ²⁰H. G. Duan, R. J. D. Miller, and M. Thorwart, *J. Phys. Chem. Lett.* **7**, 3491 (2016).
- ²¹K. Ishii, S. Takeuchi, and T. Tahara, *J. Phys. Chem. A* **112**, 2219 (2008).
- ²²P. Kambhampati, D. H. Son, T. W. Kee, and P. F. Barbara, *J. Phys. Chem. A* **104**, 10637 (2000).
- ²³J. M. Womick, B. A. West, N. F. Scherer, and A. M. Moran, *J. Phys. B: At., Mol. Opt. Phys.* **45**, 154016 (2012).
- ²⁴Y. Tanimura and R. Kubo, *J. Phys. Soc. Jpn.* **58**, 101 (1989).
- ²⁵Y. A. Yan, F. Yang, Y. Liu, and J. S. Shao, *Chem. Phys. Lett.* **395**, 216 (2004).
- ²⁶A. Ishizaki and Y. Tanimura, *J. Phys. Soc. Jpn.* **74**, 3131 (2005).
- ²⁷Y. Tanimura, *J. Phys. Soc. Jpn.* **75**, 082001 (2006).
- ²⁸Y. Tanimura, *J. Chem. Phys.* **141**, 044114 (2014).
- ²⁹Y. Tanimura, *J. Chem. Phys.* **142**, 144110 (2015).
- ³⁰R. X. Xu, P. Cui, X. Q. Li, Y. Mo, and Y. J. Yan, *J. Chem. Phys.* **122**, 041103 (2005).
- ³¹R. X. Xu and Y. J. Yan, *Phys. Rev. E* **75**, 031107 (2007).
- ³²X. Zheng *et al.*, *Prog. Chem.* **24**, 1129 (2012), available online at <http://www.progchem.ac.cn/EN/Y2012/V24/I06/1129>.
- ³³J. S. Jin, X. Zheng, and Y. J. Yan, *J. Chem. Phys.* **128**, 234703 (2008).
- ³⁴L. P. Chen, R. H. Zheng, Y. Y. Jing, and Q. Shi, *J. Chem. Phys.* **134**, 194508 (2011).
- ³⁵Y. J. Yan, *J. Chem. Phys.* **140**, 054105 (2014).
- ³⁶H. D. Zhang, R. X. Xu, X. Zheng, and Y. J. Yan, *J. Chem. Phys.* **142**, 024112 (2015).
- ³⁷J. S. Jin, S. K. Wang, X. Zheng, and Y. J. Yan, *J. Chem. Phys.* **142**, 234108 (2015).
- ³⁸R. X. Xu, B. L. Tian, J. Xu, Q. Shi, and Y. J. Yan, *J. Chem. Phys.* **131**, 214111 (2009).
- ³⁹K. B. Zhu, R. X. Xu, H. Y. Zhang, J. Hu, and Y. J. Yan, *J. Phys. Chem. B* **115**, 5678 (2011).
- ⁴⁰J. J. Ding, J. Xu, J. Hu, R. X. Xu, and Y. J. Yan, *J. Chem. Phys.* **135**, 164107 (2011).
- ⁴¹J. J. Ding, R. X. Xu, and Y. J. Yan, *J. Chem. Phys.* **136**, 224103 (2012).
- ⁴²H. D. Zhang and Y. J. Yan, *J. Chem. Phys.* **143**, 214112 (2015).
- ⁴³R. X. Xu, H. D. Zhang, X. Zheng, and Y. J. Yan, *Sci. China Chem.* **58**, 1816 (2015).
- ⁴⁴H. D. Zhang, Q. Qiao, R. X. Xu, and Y. J. Yan, "Solvent-induced polarization dynamics and coherent two-dimensional spectroscopy: Dissipation equation of motion approach," *Chem. Phys.* (in press).
- ⁴⁵G. Orlandi and W. Siebrand, *J. Chem. Phys.* **58**, 4513 (1973).
- ⁴⁶S. H. Lin and H. Eyring, *Proc. Natl. Acad. Sci. U. S. A.* **71**, 3802 (1974).
- ⁴⁷Y. Tanimura and S. Mukamel, *J. Opt. Soc. Am. B* **10**, 2263 (1993).
- ⁴⁸Y. Tanimura and S. Mukamel, *Phys. Rev. E* **47**, 118 (1993).
- ⁴⁹M. Thoss, H. B. Wang, and W. H. Miller, *J. Chem. Phys.* **115**, 2991 (2001).

- ⁵⁰U. Weiss, *Quantum Dissipative Systems*, Series in Modern Condensed Matter Physics, 3rd ed. (World Scientific, Singapore, 2008), Vol. 13.
- ⁵¹Y. J. Yan and R. X. Xu, *Annu. Rev. Phys. Chem.* **56**, 187 (2005).
- ⁵²S. Mukamel, *The Principles of Nonlinear Optical Spectroscopy* (Oxford University Press, New York, 1995).
- ⁵³J. Adolphs and T. Renger, *Biophys. J.* **91**, 2778 (2006).
- ⁵⁴C. Meier and D. J. Tannor, *J. Chem. Phys.* **111**, 3365 (1999).
- ⁵⁵H. Liu, L. L. Zhu, S. M. Bai, and Q. Shi, *J. Chem. Phys.* **140**, 134106 (2014).
- ⁵⁶R. P. Feynman and F. L. Vernon, Jr., *Ann. Phys.* **24**, 118 (1963).
- ⁵⁷J. Xu, R. X. Xu, D. Abramavicius, H. D. Zhang, and Y. J. Yan, *Chin. J. Chem. Phys.* **24**, 497 (2011).
- ⁵⁸J. Xu, H. D. Zhang, R. X. Xu, and Y. J. Yan, *J. Chem. Phys.* **138**, 024106 (2013).
- ⁵⁹S. Mukamel and D. Abramavicius, *Chem. Rev.* **104**, 2073 (2004).
- ⁶⁰S. Mukamel, Y. Tanimura, and P. Hamm, *Acc. Chem. Res.* **42**, 1207 (2009).
- ⁶¹C. Sanderson and R. Curtin, *J. Open Source Software* **1**, 26 (2016).